Research Square

Preprints are preliminary reports that have not undergone peer review.
They should not be considered conclusive, used to inform clinical practice,
or referenced by the media as validated information.

Phase-Behavior-Guided Electrodeposition of Size-Tunable Copper Pillar Arrays Using Bicontinuous Microemulsions for Cu–Cu Bonding

Jinghui Zhang
Harbin Institute of Technology
Chao Wang
Anhui Provincial Key Laboratory of Microsystems
Fengyi Wang
Harbin Institute of Technology
Jintao Wang
QianYuan Laboratory
Hongtao Chen
chenht@hit.edu.cn
Harbin Institute of Technology

Research Article

Keywords: Bicontinuous microemulsion, Phase diagram, Electrodeposition, Copper pillar arrays, Cu–Cu bonding

Posted Date: November 24th, 2026

DOI: https://doi.org/10.21203/rs.3.rs-11699800/v1

License: This work is licensed under a Creative Commons Attribution 4.0 International License.
Read Full License

Additional Declarations: No competing interests reported.

Phase-Behavior-Guided Electrodeposition of Size-Tunable Copper Pillar Arrays Using Bicontinuous Microemulsions for Cu–Cu Bonding

Jinghui Zhang[a&], Chao Wang[b&], Fengyi Wang[c], Jintao Wang[d*], Hongtao Chen[a*]

a School of Integrated Ciecuits, Harbin Institute of Technology·(Shenzhen), Shenzhen 518055, China

b Anhui Provincial Key Laboratory of Microsystems, Hefei, 230088, China

c Department of Materials Science and Engineering, Harbin Institute of Technology·(Shenzhen), Shenzhen 518055, China

d QianYuan Laboratory, HangZhou, 310000, China

* Correspondence author:

(1) Name: Jintao Wang E-mail address: jintaowcqu@foxmail.com

(2) Name: Hongtao Chen E-mail address: chenht@hit.edu.cn

& These authors contributed equally to this work and should be considered co-first authors

Abstract

Bicontinuous microemulsions (BMEs) provide a liquid soft-template platform for constructing three-dimensional Cu structures, but the relationships among BME formulation, electrochemical transport, structural confinement, and subsequent Cu–Cu bonding remain insufficiently understood. In this work, a phase-behavior-guided BME

electrodeposition strategy was developed to regulate Cu pillar arrays for pressure-assisted Cu–Cu bonding. An experimental phase diagram of the SDS/2m2b-based BME system was established to guide formulation selection, and the effects of deposition current density, water/oil balance, and surfactant/co-surfactant content were systematically investigated. A current density of 4.5 $A \cdot dm^{-2}$ enabled well-developed Cu pillars while avoiding excessive dendritic growth. Electrochemical measurements showed that the oil-rich BME exhibited higher resistivity and more restricted Cu^{2+} transport than the water-rich BME. Under galvanostatic deposition, the restricted Cu^{2+} supply would require greater cathodic polarization to sustain the imposed current density, thereby increasing the fraction of current carried by the hydrogen evolution reaction and leading to pronounced bubble-induced defects. By increasing the surfactant/co-surfactant content near the water/oil balance line, the average pillar diameter decreased from 12.20 ± 2.87 to 2.89 ± 0.70 μm, corresponding to a reduction of approximately 76%. The resulting coarse and fine Cu pillar arrays were directly bonded in air at 260°C and 8 MPa without an additional bonding material. Reducing the pillar dimensions decreased the bond-line porosity from 10.15% to 6.97% and increased the average shear strength from 36.67 ± 6.92 to 50.83 ± 8.34 MPa. These results establish a correlation among BME formulation phase diagram, electrochemical deposition, Cu pillar architecture, and bonding performance, providing a controllable route for constructing Cu-based joining interfaces for advanced electronic packaging.
Keywords: Bicontinuous microemulsion; Phase diagram; Electrodeposition; Copper pillar arrays; Cu–Cu bonding

1. Introduction

The continuous increase in device integration and power density has imposed increasingly stringent requirements on thermal management in electronic packaging.

Thermal interface materials (TIMs) are commonly introduced between heat-generating components and heat spreaders or heat sinks to reduce interfacial thermal resistance. Polymer-based TIMs are widely used because of their good conformability and processability. However, the intrinsically low thermal conductivity of most polymer matrices limits their heat-transfer capability, and thermally conductive fillers are therefore commonly incorporated to enhance effective thermal transport[1, 2]. For interfaces that must simultaneously provide mechanical attachment, heat dissipation, and electrical conduction, metallic joining materials are particularly attractive. Among them, sintered Ag nanoparticles have been extensively investigated for high-power and high-temperature die-attach applications because of their high thermal and electrical conductivities, favorable sinterability, and high-temperature service capability[3-5]. Nevertheless, the high material cost of Ag and its susceptibility to electrochemical migration have motivated increasing interest in Cu-based alternatives[6]. Cu combines high thermal and electrical conductivities with substantially lower material cost and better resistance to electrochemical migration, whereas its strong tendency toward oxidation remains a major challenge for material processing and metallurgical bonding[6-8].

For Cu-based joining, solder-free Cu–Cu bonding is attractive because it eliminates low-melting solder constituents and avoids the formation and evolution of solder-derived intermetallic compounds, while preserving the high thermal and electrical transport capability of Cu. Nevertheless, Cu–Cu direct bonding remains difficult at moderate temperatures because of the limited atomic diffusion of Cu and the presence of surface oxides[9, 10]. Cu particle sinter-joining represents another important route toward low-temperature Cu interconnection. Nano- and submicron-sized Cu particles exhibit enhanced sintering activity owing to their high surface energy and

short diffusion distances, allowing metallurgical bonding at temperatures far below the melting point of bulk Cu[7, 8, 11]. However, Cu particles are susceptible to oxidation and agglomeration, while the organic constituents required for paste dispersion and printability must be effectively removed during sintering. Incomplete removal of organics or insufficient densification may further result in residual porosity within the bonded layer, increasing the complexity of paste formulation and bonding-process control[7, 8, 11]. An alternative strategy is to directly construct three-dimensional Cu microstructures on the substrate by electrodeposition. Such preformed Cu architectures can provide numerous local contact sites and facilitate deformation and coalescence during pressure-assisted bonding without introducing a particulate bonding interlayer. Therefore, developing a simple and controllable fabrication route capable of regulating both the morphology and characteristic dimensions of these Cu structures is important for realizing this joining strategy[12, 13].

Bicontinuous microemulsions (BMEs) provide a promising soft-template platform for the controllable fabrication of three-dimensional Cu structures. A BME consists of intertwined continuous aqueous and oil domains separated by a surfactant-rich interfacial film, and its phase behavior and characteristic microstructure are highly sensitive to formulation composition[14, 15]. When the electrolyte is confined to the aqueous domains while the oil domains remain essentially nonconductive, the bicontinuous structure can spatially regulate electrodeposition by preferentially supporting ionic transport and metal growth within the aqueous network[16, 17]. In our previous work, BME-mediated electrodeposition was first employed to fabricate monolithic porous Cu films with tunable structures, which were subsequently combined with Sn for transient liquid phase interconnection[18]. The approach was then extended to the differential electrodeposition of micron-scale Cu arrays, and the resulting arrays

were evaluated as reinforcing and thermally/electrically conductive Cu frameworks in Cu–Sn transient liquid phase joints[19]. More recently, electrodeposited Cu arrays were further applied to solder-free direct Cu–Cu bonding through three-dimensional structural design[20]. These studies established the feasibility of using BME-derived Cu structures for electronic-packaging interconnections. However, the relationships among BME formulation, water/oil balance, electrochemical transport, Cu growth, and subsequent bonding behavior remain insufficiently understood. In particular, the effect of water/oil balance should be separated from that of surfactant/co-surfactant content: the former influences the proportion and transport characteristics of the conductive aqueous domains, whereas the latter can modify the stabilized oil/water interfacial area and characteristic length scale of the bicontinuous structure[14, 15]. These variations may further affect Cu^{2+} transport, hydrogen evolution, deposition morphology, and the characteristic dimensions of the resulting Cu structures. Establishing these relationships is therefore important for advancing BME electrodeposition from morphological fabrication toward controllable Cu interface engineering.

In this work, a phase-behavior-guided BME electrodeposition strategy was developed to regulate Cu pillar arrays for pressure-assisted Cu–Cu bonding. An experimental phase diagram of the SDS/2m2b-based BME system was first established to guide formulation selection. The evolution of Cu morphology with deposition current density was then investigated to identify suitable conditions for pillar formation. Subsequently, water-rich and oil-rich BMEs were compared to clarify the influence of water/oil balance on ionic transport, Cu^{2+} reduction, hydrogen evolution, and the resulting deposition morphology through electrochemical impedance spectroscopy and linear sweep voltammetry, including Cu^{2+}-free control experiments. BME formulations with different surfactant/co-surfactant contents were further selected near the water/oil

balance line to regulate the characteristic dimensions of the Cu pillars. Finally, coarse and fine Cu pillar arrays were subjected to pressure-assisted Cu–Cu bonding, and the effects of pillar dimensions on bond-line densification, fracture behavior, and shear strength were evaluated. By correlating BME phase behavior, electrochemical deposition, Cu pillar architecture, and subsequent bonding performance, this work provides a phase- behavior -guided route for the controllable construction of Cu-based joining interfaces for advanced electronic packaging.

2. Experimental

2.1 Materials and BME preparation

Copper sulfate pentahydrate ($CuSO_4 \cdot 5H_2O$, 99%), sulfuric acid (H_2SO_4, 98%), sodium sulfate (Na_2SO_4, 99%), sodium dodecyl sulfate (SDS, 99%), 2-methyl-2-butanol (2m2b, 99%), and cyclohexane (99.5%) were purchased from Innochem (China).

The preparation procedure of the bicontinuous microemulsion (BME) is schematically illustrated in Fig. 1(a). Briefly, $CuSO_4 \cdot 5H_2O$, H_2SO_4, SDS, and 2m2b were sequentially added to water and ultrasonicated in an ultrasonic bath (YL-0605) until a homogeneous aqueous precursor was obtained. Subsequently, an equal volume of cyclohexane was introduced, followed by further ultrasonication for 30 min. The resulting mixture was then allowed to stand undisturbed for approximately 30 min, during which three distinct liquid layers formed: an excess oil phase (upper layer), a middle BME phase, and an excess aqueous phase (lower layer). The middle BME phase was carefully collected for subsequent electrodeposition experiments.

To construct the BME phase diagram, the concentrations of $CuSO_4$ and H_2SO_4 in the aqueous precursor were fixed at 0.5 and 0.015 $mol \cdot L^{-1}$, respectively. At each

predetermined SDS concentration, the amount of 2m2b was systematically varied following the aforementioned preparation procedure. The compositions at which the excess aqueous phase and excess oil phase disappeared were recorded as the two boundaries of the three-phase region. By repeating this procedure at different SDS concentrations, the experimental BME phase diagram was established. The water and oil contents incorporated into the middle BME phase were determined from the changes in the volumes of the excess aqueous and oil phases relative to their initial equal volumes. The compositions at which the middle BME phase contained equal volumes of water and oil were used to define the water/oil balance line. Four representative formulations (A–D) were then selected for subsequent investigations. The concentrations of SDS and 2m2b were calculated based on the volume of the aqueous precursor prior to cyclohexane addition. For all $CuSO_4$-containing BME formulations, the base electrolyte composition was maintained constant, while only the SDS and 2m2b contents were varied.

2.2 Electrodeposition of copper pillar arrays

Copper electrodeposition was carried out using a two-electrode system with a copper plate as the anode and a copper coupon measuring 10 × 10 × 1 mm as the cathode. Prior to deposition, the copper coupons were ground with 2500-grit abrasive paper to remove surface oxides, rinsed with ethanol, and dried. Galvanostatic deposition was performed using a DC power supply (UTP1306-II, UNI-T), with the cathode fully immersed in the prepared BME. The current density was calculated based on one 10 × 10 mm cathode surface facing the anode.

The formation of copper pillar arrays through BME-mediated electrodeposition is schematically illustrated in Fig. 1(c). To investigate the effect of current density on the deposition morphology, formulation B was selected as the reference electrolyte, and the

current density was varied from 3.0 to 5.5 A·dm^{-2} at intervals of 0.5 A·dm^{-2}. For subsequent investigations into the effects of BME composition, electrodeposition using formulations A-D was conducted at 4.5 A·dm^{-2}. The deposition time was fixed at 15 min for all experiments. After deposition, the samples were rinsed with ethanol to remove residual BME and air-dried for subsequent characterization and Cu–Cu bonding.

2.3 Cu–Cu bonding

Cu–Cu direct bonding was performed using a hot-press bonding machine (CH101H-100KG), as schematically illustrated in Fig. 1(d). After electrodeposition, the 10 × 10 mm copper coupons were cut into 3 × 3 mm specimens for bonding. Two specimens bearing copper pillar arrays deposited from the same formulation were assembled face to face, allowing the opposing pillar arrays to come into direct contact. Formulations C and D were used separately to fabricate coarse- and fine-pillar joints, respectively. All samples were bonded in air at 260°C under 8 MPa for 15 min, without any additional bonding material.

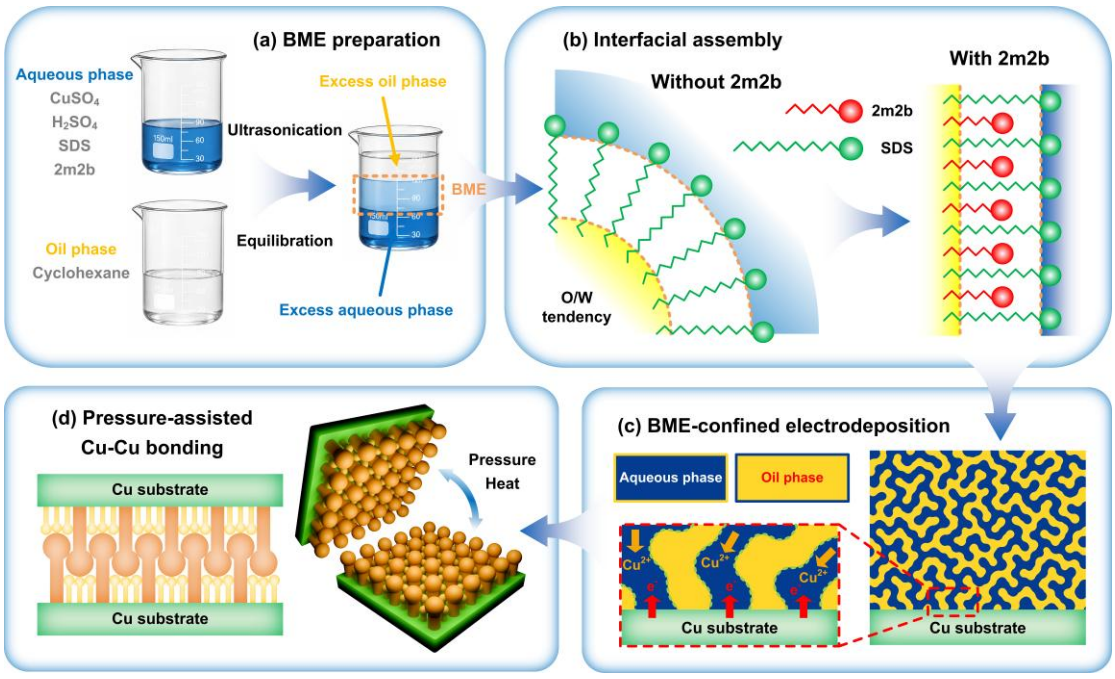

Fig. 1. Schematic illustration of BME-mediated copper pillar electrodeposition and

subsequent Cu–Cu direct bonding. (a) Preparation and phase separation of the BME system. (b) Schematic interfacial assembly of SDS and 2m2b. (c) Electrodeposition of copper pillar arrays using the middle BME phase. (d) Face-to-face assembly and pressure-assisted bonding of opposing copper pillar arrays.

2.4 Characterization and measurements

The surface morphology and cross-sectional microstructure of the electrodeposited copper pillar arrays and bonded joints were characterized by scanning electron microscopy (GeminiSEM 360, ZEISS). The diameters of copper pillars obtained from formulations C and D were measured using Nano Measurer software, with 100 pillars analyzed for each group. Transmission electron microscopy (JEM-F200, JEOL) was performed to further investigate the microstructure of copper pillars from formulation D. For TEM specimen preparation, the pillars were scraped from the substrate, ultrasonically dispersed in ethanol, and deposited onto copper grids.

Electrochemical measurements were conducted using an electrochemical workstation (CHI700E) equipped with a three-electrode system. A copper coupon, a platinum plate, and an Ag/AgCl electrode served as the working, counter, and reference electrodes, respectively. Electrochemical impedance spectroscopy (EIS) was performed at 0 V versus Ag/AgCl over a frequency range of 1 Hz to 100 kHz with an AC perturbation amplitude of 5 mV. The electrolyte resistance was determined from the real-axis intercept of the impedance spectrum. Linear sweep voltammetry (LSV) was conducted from 0.2 to -2.0 V versus Ag/AgCl at a scan rate of 0.01 $V \cdot s^{-1}$. For the Cu^{2+}-free control measurements, $CuSO_4$ was replaced with 0.333 $mol \cdot L^{-1}$ Na_2SO_4 to maintain the same total ion concentration in the aqueous precursor.

For cross-sectional characterization, the bonded joints were sequentially ground with 1200-, 2500-, and 4000-grit abrasive papers, followed by polishing with 3 and 1

μm diamond suspensions. The bond-line thickness was determined from cross-sectional SEM images, while the cross-sectional porosity was calculated using ImageJ software. The mechanical performance of the bonded joints was evaluated using a bond tester (DAGE-4000, DAGE) at a shear speed of 150 $\mu m \cdot s^{-1}$. Eight samples of each joint type were performed for shear testing, and the average results were reported. The corresponding fracture surfaces were subsequently examined by SEM.

3. Results and discussion

3.1 Phase diagram and formulation selection

The experimentally determined phase diagram of the SDS/2m2b system is presented in Fig. 2(a). With the $CuSO_4$ and H_2SO_4 concentrations held constant, a characteristic fish-shaped three-phase region was identified by varying the SDS and 2m2b contents. As the SDS concentration increased, the two phase boundaries initially diverged and subsequently converged, with the widest three-phase region appearing at approximately 0.25 $mol \cdot L^{-1}$ SDS. Notably, the water/oil balance line shifted toward higher 2m2b concentrations as the SDS concentration increased. This behavior can be attributed to the combined effects of SDS and 2m2b on the phase behavior of the BME. While increasing the SDS content enhances the hydrophilic tendency of the system, increasing the 2m2b content shifts the phase balance toward the oil-rich side. Consequently, a higher 2m2b concentration is required as the SDS content increases to maintain a balanced water/oil composition in the middle BME phase[14, 21, 22].

Based on the established phase diagram, formulations A and B were selected at a fixed SDS concentration of 0.25 $mol \cdot L^{-1}$ to investigate the influence of water/oil balance on electrodeposition behavior. As shown in Fig. 2(b), increasing the 2m2b concentration from 1.05 $mol \cdot L^{-1}$ in formulation B to 1.45 $mol \cdot L^{-1}$ in formulation A

shifted the middle BME phase from a water-rich to an oil-rich composition. The corresponding water/oil proportions were 68/32 and 35/65 for formulations B and A, respectively. This compositional difference provided a basis for comparing the electrochemical behavior and copper deposition morphology under different water/oil conditions.

Formulations C and D were further selected near the water/oil balance line, with SDS concentrations of 0.12 and 0.42 mol·L^{-1} and corresponding 2m2b concentrations of 1.25 and 1.30 mol·L^{-1}, respectively. These formulations were designed to investigate the influence of surfactant and co-surfactant contents on copper pillar morphology while maintaining a relatively balanced water/oil composition. The compositions of all four formulations are summarized in Fig. 2(c).

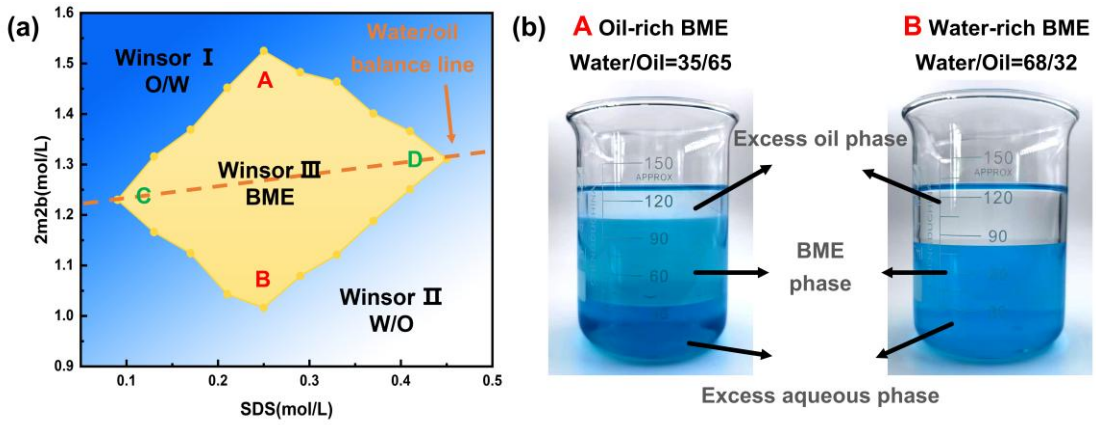

(c)

	A	B	C	D
SDS(mol·L^{-1})	0.25	0.25	0.12	0.42
2m2b(mol·L^{-1})	1.45	1.05	1.25	1.30

Fig. 2. Phase diagram and formulation design of the BME system. (a) Experimental phase diagram of the SDS/2m2b system. (b) Photographs of the phase-separated formulations A and B. (c) Compositions of the selected BME formulations.

3.2 Effect of current density on copper electrodeposition

The influence of current density on copper electrodeposition was first investigated using formulation B, with the deposition time fixed at 15 min. Fig. 3 shows the

morphological evolution of the copper deposits as the current density increased from 3.0 to 5.5 $A \cdot dm^{-2}$. At 3.0 $A \cdot dm^{-2}$, only slight surface undulations were observed, without the formation of distinct copper pillars. When the current density increased to 3.5 $A \cdot dm^{-2}$, granular deposits began to emerge on the substrate surface, followed by the initial growth of columnar structures at 4.0 $A \cdot dm^{-2}$. At 4.5 $A \cdot dm^{-2}$, the copper pillars became more developed, with flower-like features appearing at their tips. Further increasing the current density to 5.0 and 5.5 $A \cdot dm^{-2}$ resulted in a substantial increase in deposit size, accompanied by pronounced branching and dendritic growth.

This morphological evolution can be associated with the enhanced copper deposition rate at higher current densities. While increasing the current density promotes pillar growth, excessively high values may intensify local Cu^{2+} depletion and favor preferential deposition at protruding regions, leading to dendritic structures[23, 24]. Considering that the copper pillars are intended for subsequent pressure-assisted Cu–Cu bonding, their morphology should provide sufficient height and structural integrity to promote effective contact and deformation during bonding. The short pillars formed at 4.0 $A \cdot dm^{-2}$ provide limited contact, whereas the loosely branched dendritic deposits formed above 5.0 $A \cdot dm^{-2}$ are structurally unfavorable under pressure. Accordingly, 4.5 $A \cdot dm^{-2}$ was selected for subsequent experiments, providing sufficiently developed copper pillars with flower-like terminations while avoiding excessive dendritic growth.

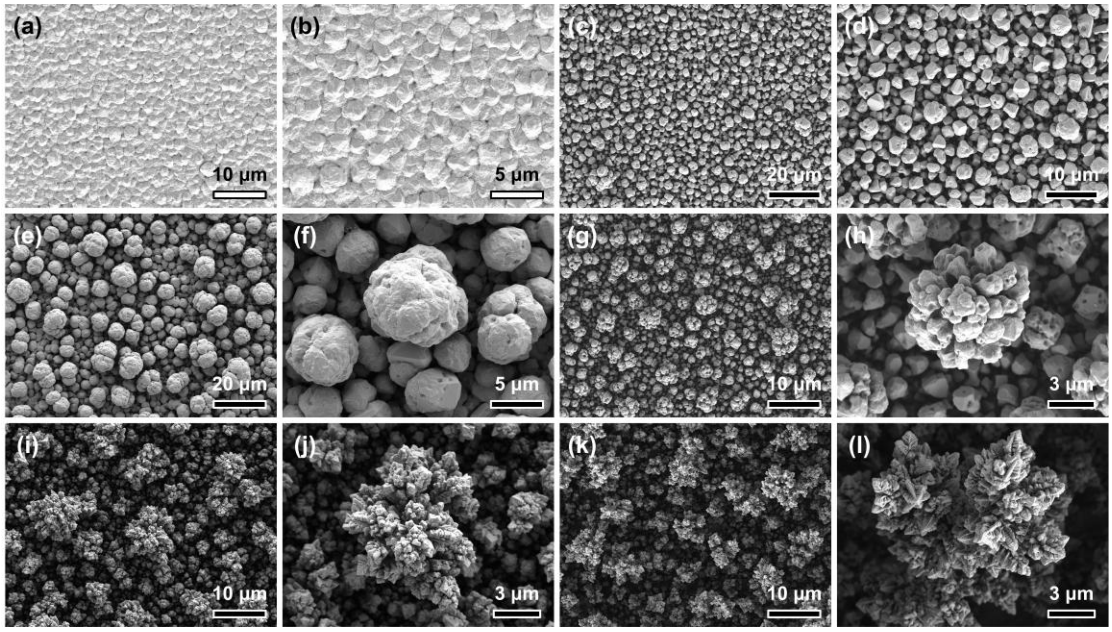

Fig. 3. SEM images showing the morphological evolution of copper deposits obtained from formulation B at different current densities: (a, b) 3.0, (c, d) 3.5, (e, f) 4.0, (g, h) 4.5, (i, j) 5.0, and (k, l) 5.5 $A \cdot dm^{-2}$. The deposition time was fixed at 15 min for all samples.

3.3 Effect of water/oil balance on copper electrodeposition

To investigate the influence of water/oil balance on copper electrodeposition, formulations A and B were compared under identical deposition conditions. As shown in Fig. 4, the oil-rich BME produced a relatively irregular copper pillar array, accompanied by numerous circular pores induced by hydrogen bubbles. These bubbles can locally mask the cathode surface and interrupt copper growth, resulting in discontinuous deposition[25]. In contrast, the water-rich BME yielded a denser and more well-defined copper pillar array, with fewer bubble-induced defects, indicating more favorable conditions for copper pillar formation.

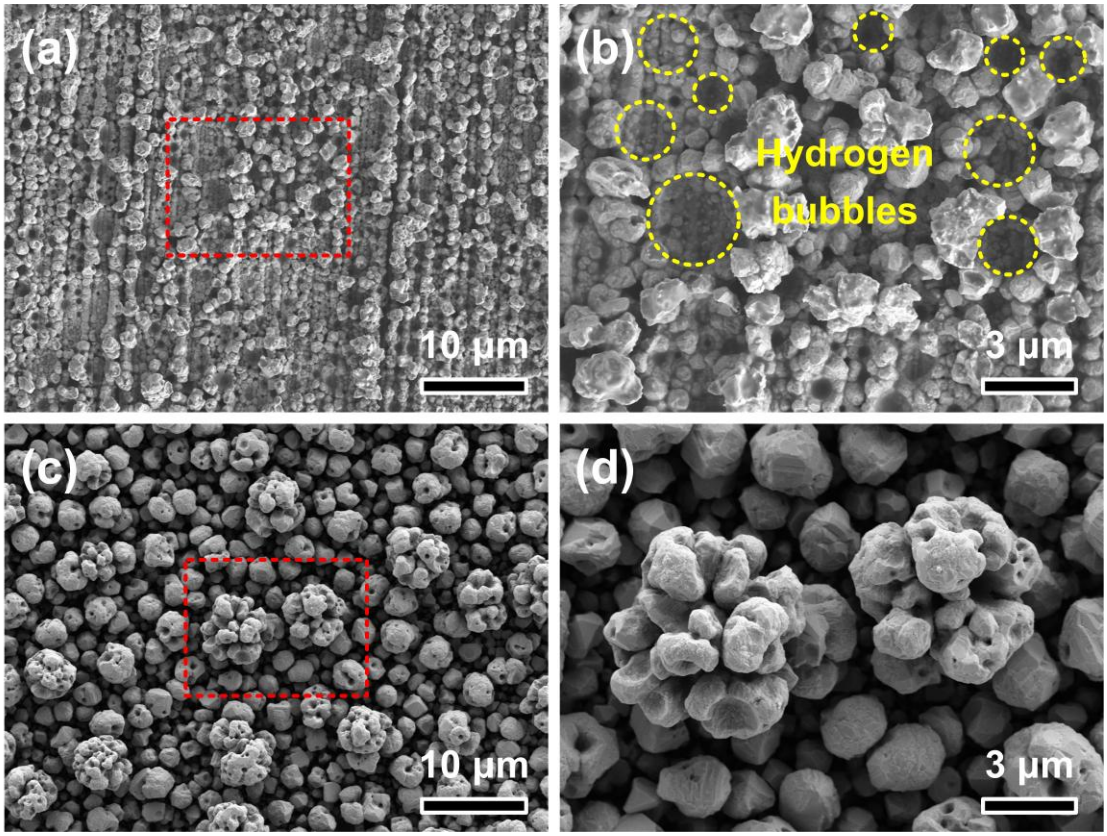

Fig. 4. SEM images of copper pillar arrays electrodeposited at 4.5 A·dm^{-2} for 15 min. (a, b) Oil-rich BME, formulation A. (c, d) Water-rich BME, formulation B.

To further understand these morphological differences, electrochemical measurements were performed using the aqueous electrolyte and the two BME formulations. The Bode plots in Fig. 5(a, b) reveal distinct impedance responses among the three electrolytes. At lower frequencies, the phase angles approach 0°, indicating a predominantly resistive impedance response. The resistivity values summarized in the inset of Fig. 5(a) increase in the order of aqueous electrolyte, water-rich BME, and oil-rich BME. This trend can be associated with the reduced proportion of the conductive aqueous phase in the BME, which makes ionic transport less favorable. The higher resistivity of the oil-rich formulation reflects less favorable ionic transport, which can limit the continuous supply of Cu^{2+} to the cathode during electrodeposition.

The cathodic polarization curves of the $CuSO_4$-containing BMEs are presented in

Fig. 5(c). The water-rich formulation exhibits a distinct current plateau at approximately 4.5 $A \cdot dm^{-2}$, suggesting that Cu^{2+} reduction approaches a mass-transport-limited regime[23, 25]. Notably, this value corresponds closely to the current density selected for copper pillar electrodeposition in Section 3.2. In comparison, the oil-rich BME exhibits a substantially suppressed cathodic response and does not reach the selected deposition current density within the investigated potential range, reflecting more restricted electrochemical transport conditions.

Since the measured cathodic current in $CuSO_4$-containing BMEs includes contributions from both Cu^{2+} reduction and hydrogen evolution, additional LSV measurements were conducted using Cu^{2+}-free BMEs to eliminate the interference from copper deposition. As shown in Fig. 5(d), the water-rich formulation exhibits a higher HER-related current than the oil-rich formulation at the same applied potential. This result is consistent with the more favorable ionic transport conditions in the water-rich BME and indicates that the pronounced hydrogen-bubble defects observed in the oil-rich deposits cannot be simply attributed to a higher HER response at an identical potential. However, the actual electrodeposition experiments were performed under galvanostatic conditions. Owing to the more restricted Cu^{2+} supply in the oil-rich BME, greater cathodic polarization may be required to sustain the applied current density of 4.5 $A \cdot dm^{-2}$, thereby increasing the relative contribution of HER to the total current. The resulting hydrogen bubbles can obstruct local copper growth, providing an explanation for the poorer pillar formation and more pronounced deposition defects observed in the oil-rich formulation.

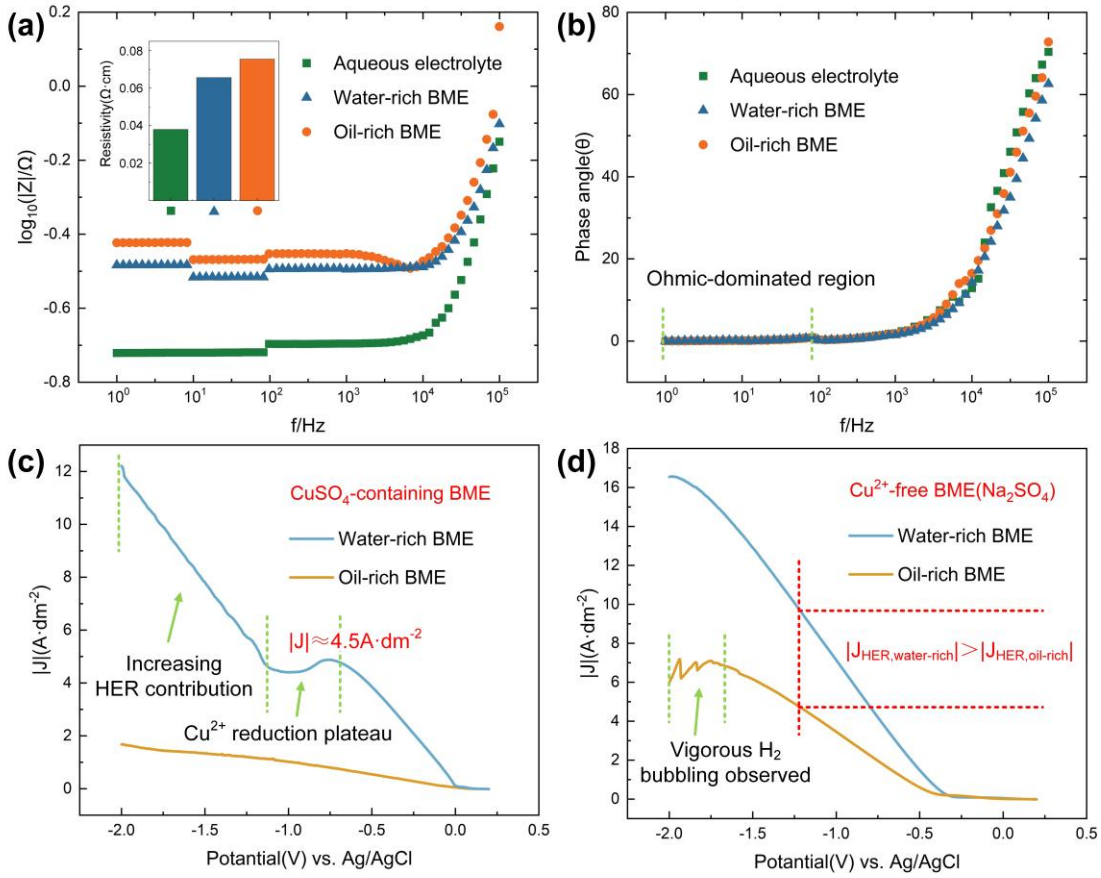

Fig. 5. Electrochemical characterization of the aqueous electrolyte and BME systems. (a) Bode impedance magnitude plots with an inset showing the calculated resistivity. (b) Bode phase angle plots. (c) LSV curves of $CuSO_4$-containing BMEs. (d) LSV curves of Cu^{2+}-free BMEs prepared using Na_2SO_4.

3.4 Composition-regulated morphology and microstructure of copper pillars

The influence of BME composition on copper pillar morphology was further investigated using formulations C and D selected near the water/oil balance line. As shown in Fig. 6(a, b), formulation C produced relatively coarse pillars with pronounced flower-like terminations and a broad absolute diameter distribution. In contrast, formulation D generated a much denser array of fine pillars with a narrower absolute diameter distribution and a characteristic pagoda-like morphology, as shown in Fig. 6(d, e). Statistical analysis confirms this pronounced dimensional refinement: the average

pillar diameter decreased from 12.20 ± 2.87 μm for formulation C to 2.89 ± 0.70 μm for formulation D, corresponding to a reduction of approximately 76%.

The substantial change in pillar dimensions can be related to the increased contents of SDS and 2m2b in formulation D. Under a relatively balanced water/oil composition, a larger amount of surfactant and co-surfactant can stabilize a greater oil/water interfacial area within a given BME volume. The increased interfacial area may correspond to a reduced characteristic width of the interconnected aqueous domains, thereby imposing stronger spatial confinement on copper growth[15, 26, 27]. Such confinement suppresses unrestricted lateral expansion and branching of the deposits, leading to the transition from the coarse flower-like structures in formulation C to the finer and more compact pagoda-like pillars in formulation D. These results demonstrate that the dimensions and morphology of the electrodeposited copper pillars can be effectively regulated through the surfactant/co-surfactant composition of the BME.

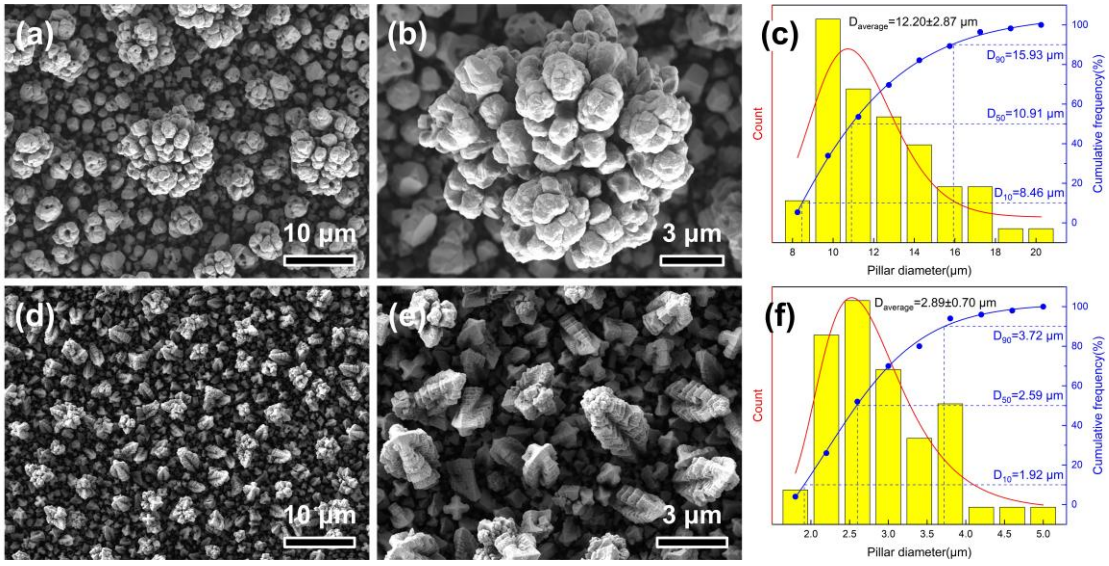

Fig. 6. Morphology and diameter distributions of copper pillars electrodeposited from formulations C and D. (a, b) SEM images of the coarse flower-like pillars obtained from formulation C. (c) Corresponding diameter distribution and cumulative frequency curve of formulation C. (d, e) SEM images of the fine pagoda-like pillars

obtained from formulation D. (f) Corresponding diameter distribution and cumulative frequency curve of formulation D.

The microstructure of the fine copper pillars obtained from formulation D was further examined by TEM, as shown in Fig. 7. The low-magnification images in Fig. 7(a, b) show a stepped and faceted pagoda-like profile consistent with the morphology observed by SEM. HRTEM analysis reveals different crystallographic features between the interior and outer regions of the pillar. A lattice spacing of 0.208 nm observed in the inner region corresponds to the Cu (111) planes, whereas a spacing of 0.181 nm in the outer region is assigned to Cu (200). This spatial variation suggests that copper growth does not proceed with a single crystallographic orientation throughout the pillar, but undergoes a local orientation evolution as deposition progresses. The changing electrochemical environment at the growing surface, together with the geometric confinement imposed by the BME, may contribute to this orientation variation[28, 29].

Twin lamellae are also clearly observed in the local region shown in Fig. 7(f), revealing the formation of twinned domains during electrodeposition. The SAED pattern in Fig. 7(g) consists of discrete diffraction spots distributed along the Cu (111) and (200) rings, indicating the presence of multiple crystallographic domains rather than a single-crystalline structure. Together, the locally distinct crystallographic orientations, twin lamellae, and spotty ring-like SAED pattern reveal a multidomain microstructure within the fine copper pillars.

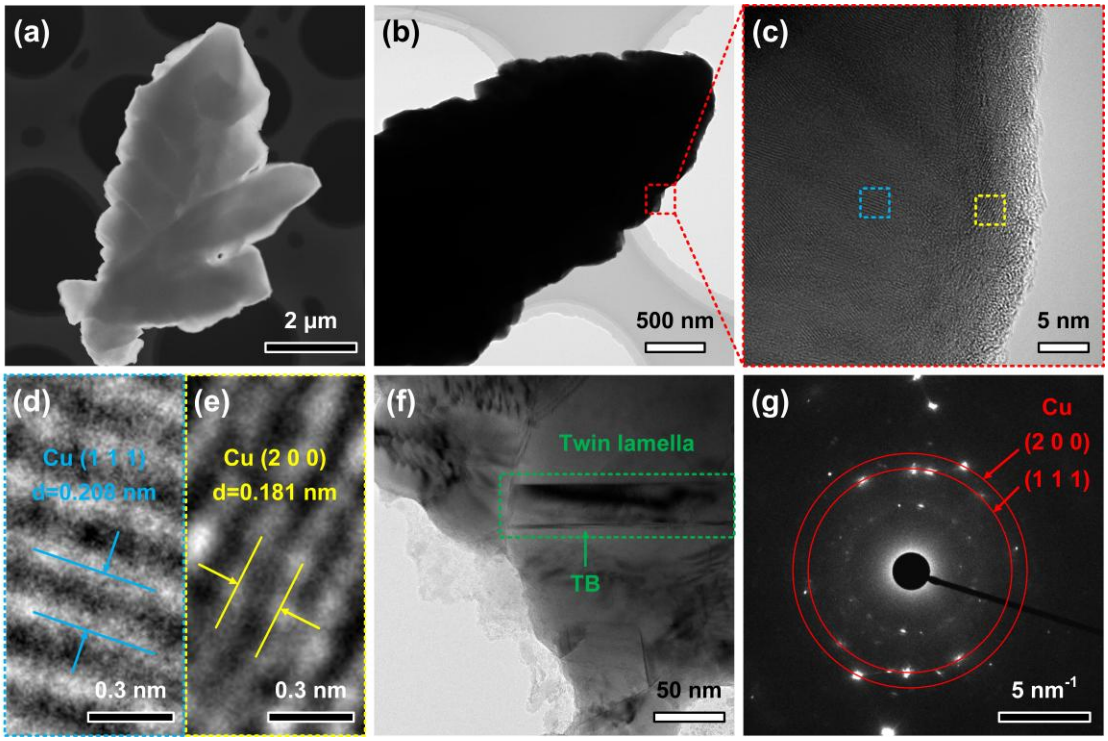

Fig. 7. TEM characterization of copper pillars obtained from formulation D. (a, b) Low-magnification TEM images showing the overall morphology of the copper pillars. (c–e) HRTEM images of selected regions with lattice spacings corresponding to Cu (111) and Cu (200). (f) TEM image showing local twin lamellae. (g) SAED pattern of the electrodeposited copper.

3.5 Cu–Cu bonding behavior and mechanical performance

The influence of copper pillar dimensions on Cu–Cu bonding was evaluated using the coarse pillars from formulation C and the fine pillars from formulation D under identical bonding conditions. As shown in Fig. 8, both pillar arrays formed continuous bond lines after hot pressing, but clear differences were observed in the joint microstructure. The coarse-pillar joint exhibited a bond-line thickness of approximately 11.12 μm and a cross-sectional porosity of 10.15%, with several residual voids remaining within the bond line. In comparison, the fine-pillar joint showed a thinner and more compact bond line of approximately 8.63 μm, while the porosity decreased to 6.97%. The finer pillars therefore produced a more continuous bond line with fewer

residual defects.

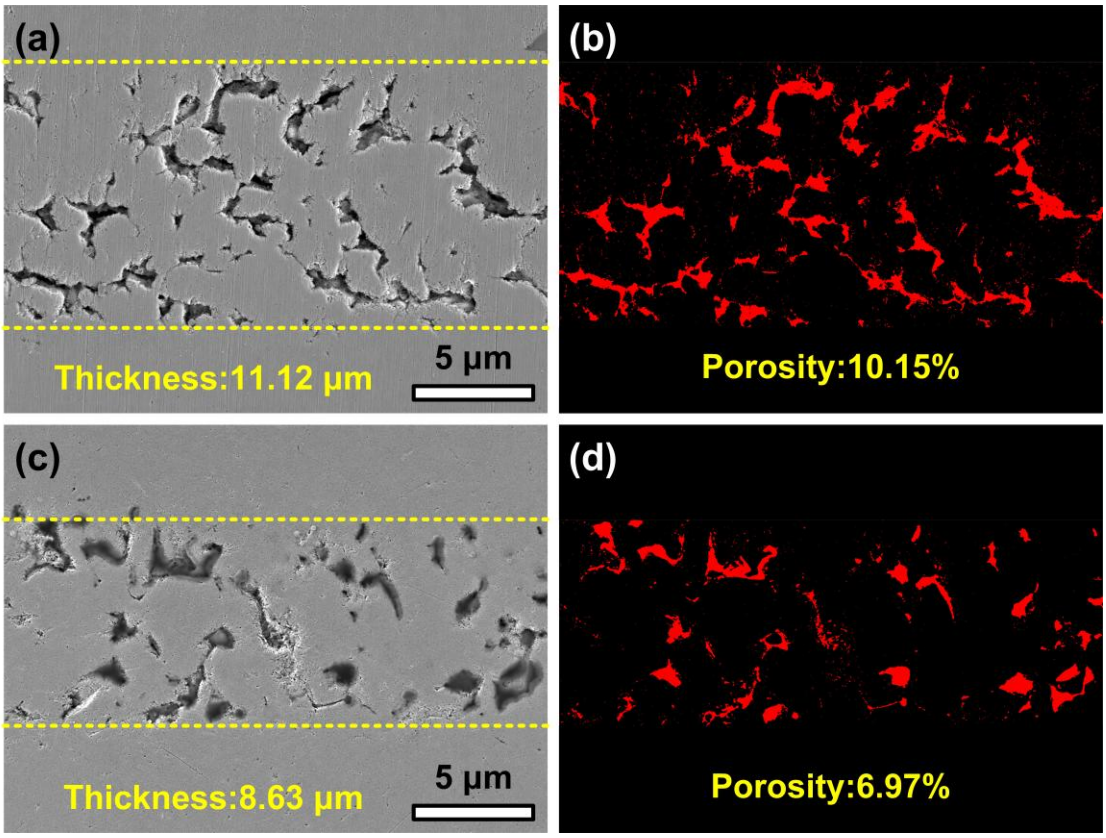

Fig. 8. Cross-sectional morphology and porosity analysis of Cu–Cu joints fabricated using coarse and fine copper pillars. (a, b) Cross-sectional SEM image and corresponding binarized image of the coarse-pillar joint. (c, d) Cross-sectional SEM image and corresponding binarized image of the fine-pillar joint.

The improved densification of the fine-pillar joint can be attributed to its higher pillar density and smaller characteristic dimensions. During hot pressing, the denser array provides more contact sites between the opposing copper pillars, while the smaller pillar dimensions facilitate local deformation and intimate contact under the applied pressure. These effects facilitate the progressive coalescence of adjacent copper structures and reduce the residual void volume within the bond line[9, 30]. In contrast, the coarse pillars provide fewer effective contact sites, making complete coalescence more difficult under the same bonding conditions.

The differences in bonding quality are further reflected in the shear strength and

fracture morphologies shown in Fig. 9. The average shear strength increased from 36.67 ± 6.92 MPa for the coarse-pillar joint to 50.83 ± 8.34 MPa for the fine-pillar joint, corresponding to an improvement of approximately 38.6%. The fracture surface of the coarse-pillar joint shows recognizable pillar remnants and local regions of incomplete coalescence, as shown in Fig. 9(b). In contrast, the fine-pillar joint exhibits a more continuous fracture morphology with pronounced ligaments and dimples, indicating more extensive plastic deformation during fracture.

For both joints, fracture predominantly occurred within the copper pillar layer rather than along the pillar/substrate interface, as schematically illustrated in Fig. 9(f). This cohesive fracture mode indicates that the pillar/substrate interface was not the weakest region of the joint. Combined with the lower porosity and higher shear strength of the fine-pillar joint, these results demonstrate that reducing the pillar dimensions promotes more complete coalescence during pressure-assisted bonding and improves the mechanical integrity of the Cu–Cu joint.

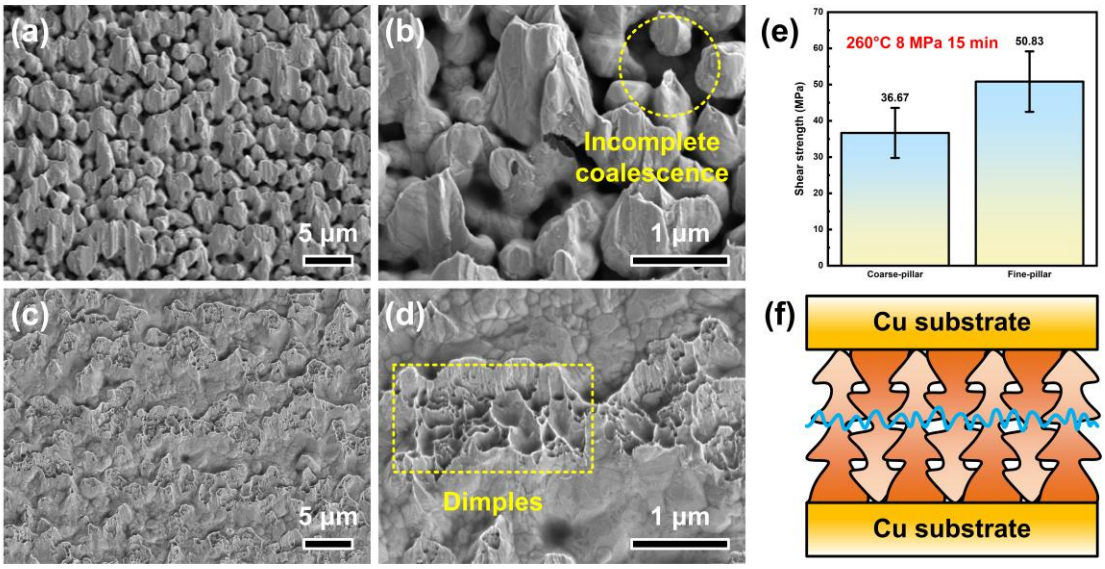

Fig. 9. Fracture morphologies and shear performance of Cu–Cu joints fabricated using coarse and fine copper pillars. (a, b) Fracture surfaces of the coarse-pillar joint at different magnifications. (c, d) Fracture surfaces of the fine-pillar joint at different

magnifications. (e) Shear strength of the two joints. (f) Schematic illustration of fracture within the copper pillar layer for both joints.

4. Conclusions

A phase- diagram -guided BME electrodeposition strategy was developed for the controlled fabrication of Cu pillar arrays and their subsequent pressure-assisted Cu–Cu bonding. The experimental phase diagram enabled the effects of water/oil balance and surfactant/co-surfactant content to be distinguished. The evolution of deposition morphology with current density showed that 4.5 $A \cdot dm^{-2}$ provided an appropriate balance between pillar development and suppression of excessive dendritic growth. Comparison of water-rich and oil-rich BMEs demonstrated that the water/oil balance strongly affected electrochemical transport. The oil-rich BME exhibited higher resistivity and more restricted Cu^{2+} supply. Under galvanostatic conditions, sustaining the imposed current density would therefore require greater cathodic polarization, increasing the fraction of current carried by hydrogen evolution and resulting in more pronounced bubble-induced defects. In contrast, regulation of the surfactant/co-surfactant content near the water/oil balance line provided an effective means of controlling the characteristic pillar dimensions. Increasing these contents reduced the average Cu pillar diameter from 12.20 ± 2.87 to 2.89 ± 0.70 μm and produced dense pagoda-like pillar arrays. The finer pillar architecture facilitated local contact and deformation during hot pressing, promoting progressive coalescence and bond-line densification. Consequently, the cross-sectional porosity decreased from 10.15% to 6.97%, while the average shear strength increased from 36.67 ± 6.92 to 50.83 ± 8.34 MPa, corresponding to an improvement of approximately 38.6%. Fracture occurred predominantly within the Cu pillar layer rather than along the pillar/substrate interface for both joints. Overall, the results demonstrate that phase-behavior-guided BME

formulation can be used to regulate electrochemical deposition and Cu pillar dimensions, which in turn govern the densification and mechanical integrity of Cu–Cu joints. This phase-behavior-guided strategy provides a controllable approach for constructing three-dimensional Cu joining interfaces for advanced electronic packaging.

Declaration of competing interest

The authors declare that they have no known competing financial interests or personal relationships that could have appeared to influence the work reported in this paper.

Acknowledgements

This work is financially supported by Special Funds for the Cultivation of Guangdong College Students' Scientific and Technological Innovation (Grant No. pdjh2026bk239).

References

[1] DAI W, WANG Y D, LI M H, et al. 2D Materials-Based Thermal Interface Materials: Structure, Properties, and Applications [J]. Advanced Materials, 2024, 36(37).

[2] FENG C P, YANG L Y, YANG J, et al. Recent advances in polymer-based thermal interface materials for thermal management: A mini-review [J]. Composites Communications, 2020, 22.

[3] PAKNEJAD S A, MANNAN S H. Review of silver nanoparticle based die attach materials for high power/temperature applications [J]. Microelectronics Reliability, 2017, 70: 1-11.

[4] SIOW K S. Are Sintered Silver Joints Ready for Use as Interconnect Material in Microelectronic Packaging? [J]. Journal of Electronic Materials, 2014, 43(4): 947-61.

[5] WAKAMOTO K, NAMAZU T. Mechanical Characterization of Sintered Silver

Materials for Power Device Packaging: A Review [J]. Energies, 2024, 17(16).
[6] CHEN T F, SIOW K S. Comparing the mechanical and thermal-electrical properties of sintered copper (Cu) and sintered silver (Ag) joints [J]. Journal of Alloys and Compounds, 2021, 866.
[7] WANG Y J, XU D, YAN H D, et al. Low-temperature copper sinter-joining technology for power electronics packaging: A review [J]. Journal of Materials Processing Technology, 2024, 332.
[8] ZHANG B Y, DAMIAN A, ZIJL J, et al. In-air sintering of copper nanoparticle paste with pressure-assistance for die attachment in high power electronics [J]. Journal of Materials Science-Materials in Electronics, 2021, 32(4): 4544-55.
[9] HE C, ZHOU J Z, ZHOU R, et al. Nanocrystalline copper for direct copper-to-copper bonding with improved cross-interface formation at low thermal budget [J]. Nature Communications, 2024, 15(1).
[10] ZHAO Z H, GAO L Y, LIU Z Q. Review of Cu-Cu direct bonding technology in advanced packaging [J]. Nanotechnology, 2025, 36(26).
[11] YOON J W, BACK J H. Effect of Sintering Conditions on the Mechanical Strength of Cu-Sintered Joints for High-Power Applications [J]. Materials, 2018, 11(11).
[12] BICKEL S, QUEDNAU S, BIRLEM O, et al. Fine-Pitch Copper Nanowire Interconnects for 2.5/3D System Integration [J]. Journal of Electronic Materials, 2024, 53(8): 4410-20.
[13] JIANG H, ROBERTSON S, LIANG S B, et al. Rapid formation of intermetallic joint using Cu-Sn nanocomposite interlayer based on patterned copper nanowire array [J]. Materials Letters, 2022, 307.
[14] SALAGER J L, MARQUEZ R, RONDóN M, et al. Review on Some Confusion Produced by the Bicontinuous Microemulsion Terminology and Its Domains Microcurvature: A Simple Spatiotemporal Model at Optimum Formulation of Surfactant-Oil-Water Systems [J]. Acs Omega, 2023, 8(10): 9040-57.
[15] TARTARO G, MATEOS H, SCHIRONE D, et al. Microemulsion Microstructure(s): A Tutorial Review [J]. Nanomaterials, 2020, 10(9).
[16] SERRà A, GóMEZ E, CALDERó G, et al. Microemulsions for obtaining nanostructures by means of electrodeposition method [J]. Electrochemistry Communications, 2013, 27: 14-8.
[17] SILLER-MARTINEZ A S, FUENTES K M, ADESUJI E T, et al. Biomimetic Hierarchical Superstructures: Approaches Using Bicontinuous Microemulsions

and Electrodeposition [J]. Frontiers in Materials, 2022, 9.
[18] WANG F Y, LV Z W, ZHONG X X, et al. Soft-template-assisted bottom-up fabrication of tunable porosity monolithic copper film for interconnection in microelectronics [J]. Journal of the Taiwan Institute of Chemical Engineers, 2023, 152.
[19] WANG F Y, LI X J, LIU J H, et al. Cu array fabrication: An environmentally sustainable approach through bicontinuous microemulsion differential electrodeposition for advanced power device packaging [J]. Journal of the Taiwan Institute of Chemical Engineers, 2024, 162.
[20] WANG F Y, ZHANG J H, ZHANG Y H, et al. Inspired by mortise-tenon structure: 3D interlocking design for direct Cu bonding of cu arrays without solder [J]. Journal of Materials Science-Materials in Electronics, 2025, 36(28).
[21] KEGEL W K, LEKKERKERKER H N W. PHASE-BEHAVIOR OF AN IONIC MICROEMULSION SYSTEM AS A FUNCTION OF THE COSURFACTANT CHAIN-LENGTH [J]. Colloids and Surfaces a-Physicochemical and Engineering Aspects, 1993, 76: 241-8.
[22] MISHRA B K, VALAULIKAR B S, KUNJAPPU J T, et al. INFLUENCE OF MICROEMULSION STRUCTURE ON REACTION-RATES [J]. Journal of Colloid and Interface Science, 1989, 127(2): 373-6.
[23] NIKOLIC N D, POPOV K I, PAVLOVIC L J, et al. Morphologies of copper deposits obtained by the electrodeposition at high overpotentials [J]. Surface & Coatings Technology, 2006, 201(3-4): 560-6.
[24] NISHIKAWA K, CHASSAING E, ROSSO M. In situ concentration measurements around the transition between two dendritic growth regimes [J]. Electrochimica Acta, 2011, 56(16): 5464-71.
[25] NIKOLIC N D, PAVJOVIC L J, PAVLOVIC M G, et al. Formation of dish-like holes and a channel structure in electrodeposition of copper under hydrogen co-deposition [J]. Electrochimica Acta, 2007, 52(28): 8096-104.
[26] MULDER M, LI X S X, NAZIM M M, et al. Systematically quantifying oil-water microemulsion structures using (spin-echo) small angle neutron scattering [J]. Colloids and Surfaces a-Physicochemical and Engineering Aspects, 2019, 575: 166-75.
[27] ZEMB T. Flexibility, persistence length and bicontinuous microstructures in microemulsions [J]. Comptes Rendus Chimie, 2009, 12(1-2): 218-24.

546 [28] HASEGAWA M, MIESZALA M, ZHANG Y C, et al. Orientation-controlled
547 nanotwinned copper prepared by electrodeposition [J]. Electrochimica Acta, 2015,
548 178: 458-67.
549 [29] ZHANG X Y, YUAN L F, LEI Y, et al. Electrochemical gradients driven 3D
550 printing of nano-twinned copper structures by direct current dynamic meniscus
551 confined electrodeposition [J]. Applied Materials Today, 2021, 24.
552 [30] JUANG J Y, LU C L, LI Y J, et al. Correlation between the Microstructures of
553 Bonding Interfaces and the Shear Strength of Cu-to-Cu Joints Using (111)-
554 Oriented and Nanotwinned Cu [J]. Materials, 2018, 11(12).
555